Raman scattering intensities in $BaTiO_3$ and $PbTiO_3$ prototypical ferroelectrics from density functional theory

2009 J. Phys.: Condens. Matter 21 215901

(http://iopscience.iop.org/0953-8984/21/21/215901)

IOP PUBLISHING JOURNAL OF PHYSICS: CONDENSED MATTER

J. Phys.: Condens. Matter **21** (2009) 215901 (10pp) doi:10.1088/0953-8984/21/21/215901

Raman scattering intensities in $BaTiO_3$ and $PbTiO_3$ prototypical ferroelectrics from density functional theory

P Hermet[1], **M Veithen and Ph Ghosez**

Physique Théorique des Matériaux, Université de Liège, B-5, B-4000 Sart-Tilman, Belgium

E-mail: patrick.hermet@hotmail.fr

Received 22 December 2008, in final form 3 April 2009
Published 29 April 2009
Online at stacks.iop.org/JPhysCM/21/215901

Abstract

Nonlinear optical susceptibilities and Raman scattering spectra of the ferroelectric phases of $BaTiO_3$ and $PbTiO_3$ are computed using a first-principles approach based on density functional theory and taking advantage of a recent implementation based on the nonlinear response formalism and the $2n + 1$ theorem. These two prototypical ferroelectric compounds were chosen to demonstrate the accuracy of the Raman calculation based both on their complexity and their technological importance. The computation of the Raman scattering intensities has been performed not only for the transverse optical modes, but also for the longitudinal optical ones. The agreement between the measured and computed Raman spectra of these prototypical ferroelectrics is remarkable for both the frequency position and the intensity of Raman lines. This agreement presently demonstrates the state-of-the-art in the computation of Raman responses on one of the most complex systems, ferroelectrics, and constitutes a step forward in the reliable prediction of their electro-optical responses.

1. Introduction

Raman spectroscopy is a powerful experimental tool, nowadays routinely applied for the characterization of material properties [1–7]. The interpretation of the positions and intensities of Raman lines is usually not straightforward and calls for accurate theoretical support. While density functional theory (DFT) is routinely used for the determination of vibrational frequencies, its application to compute Raman intensities remains challenging, mainly because of the huge computational effort required in the calculation of the Raman susceptibility tensors. For this reason, theoretical investigations have usually been based on empirical or semi-empirical approaches, such as the bond polarizability model [8–10]. These models generally rely on a description of the dielectric response in terms of contributions of individual bonds and their empirical parameters are obtained by considering experimental data of representative systems. The main advantage of these models over first-principles approaches is their ease of implementation, their low computational cost and their ability to tackle large and complex structures. However, these models are usually less accurate and their parameters are rarely transferable [8]. Furthermore, in the case of ABO_3 compounds with a rather ionic bonding, their applications are not straightforward.

In this paper, we investigate the nonlinear optical coefficients and the Raman spectra of the $BaTiO_3$ and $PbTiO_3$ prototypical ferroelectrics using DFT and taking advantage of a recent implementation based on the nonlinear response formalism and the $2n + 1$ theorem [11]. The computation of the intensity of the Raman lines is performed not only for the transverse optical (TO) modes, but also for the longitudinal optical (LO) ones.

The motivation in the investigation of $BaTiO_3$ and $PbTiO_3$ prototypical ferroelectrics is threefold. First, Raman spectra of $BaTiO_3$ and $PbTiO_3$ have never been reported in the literature using first-principles methods. The good agreement between their calculated spectra and the experimental ones demonstrates the accuracy of the computational method in complex oxide materials. Then, we have calculated the rhombohedral phase of $BaTiO_3$ for which few experimental data are available [12, 13], and none of them on the

[1] Author to whom any correspondence should be addressed. Present address: Laboratoire de Physique du Solide, Facultés Universitaires Notre-Dame de la Paix, B-5000 Namur, Belgium.

monocrystal. Finally, our method provides access to the microscopic parameters involved in the Raman response and allows us to clarify the quite different behavior of both these compounds.

This paper is organized as follows. Sections 2 and 3, respectively, describe the formalism and the computational parameters used to compute the Raman spectra of $BaTiO_3$ and $PbTiO_3$ ferroelectric phases using first principles. In sections 4–8, we respectively present the structure, the nonlinear optical susceptibility tensors, the electronic dielectric and dynamical charge tensors, a phonon analysis including LO–TO splittings, and the derivatives of the linear dielectric susceptibility tensor with respect to atomic displacements. These quantities are all the ingredients required to compute the Raman spectra. Section 9 is devoted to the comparison between our calculated Raman spectra of $BaTiO_3$ and $PbTiO_3$ and the experimental ones. Finally, section 10 discusses the transferability of the calculated Raman quantities and section 11 concludes the paper.

2. Theoretical section

In this section, we give the formalism that we have used for the calculation of Raman activities. We only focus on first-order processes, which involve a single-phonon excitation. The momentum conservation imposes that only phonons of wavevectors, $\mathbf{q}$, close to the center of the Brillouin zone can be excited. In practice, adopting the dipole approximation, we only consider zone-center phonons ($\mathbf{q} = \mathbf{0}$) and account for the dependence on the direction of $\mathbf{q}$ resulting from the long-range nature of the Coulomb field in polar materials.

2.1. Dynamical matrix

In the limit $\mathbf{q} \to \mathbf{0}$, the dynamical matrix, D, can be expressed as the sum of an analytical part (AN) and a non-analytical part (NA) [14]:

$$D_{\alpha\beta,\kappa\kappa'}(\mathbf{q} \to \mathbf{0}) = D^{\mathrm{AN}}_{\alpha\beta,\kappa\kappa'}(\mathbf{q} = \mathbf{0}) + D^{\mathrm{NA}}_{\alpha\beta,\kappa\kappa'}(\mathbf{q} \to \mathbf{0}), \quad (1)$$

where the (α, β) and (κ, κ') indices run over the Cartesian directions and the atoms in the primitive unit cell, respectively. The analytical part corresponds to the second-order derivatives of the energy with respect to atomic displacements at $\mathbf{q} = \mathbf{0}$ under the condition of vanishing macroscopic electric field. The second term is due to the long-range electrostatic interactions in polar crystals. It is at the origin of the so-called LO–TO splitting and can be computed from knowledge of the Born effective charges, Z^*, and the electronic dielectric tensor, ϵ^∞, as described in [14]. The phonon frequencies, ω_m, and the eigendisplacement vectors, $U_m(\alpha\kappa)$, of the mth zone-center phonon mode are solutions of the following generalized eigenvalue problem:

$$\sum_{\beta,\kappa'} D_{\alpha\beta,\kappa\kappa'} U_m(\beta\kappa') = M_\kappa \omega_m^2 U_m(\alpha\kappa), \quad (2)$$

where M_κ is the mass of the κth atom. As a convention, we choose the eigendisplacement vectors to be normalized as

$$\sum_{\alpha,\kappa} M_\kappa U_m(\alpha\kappa) U_n(\alpha\kappa) = \delta_{mn}. \quad (3)$$

2.2. Nonresonant Raman scattering

The nonresonant Raman scattering efficiency in a given direction, with a frequency between ω_d and $\omega_d + \mathrm{d}\omega_d$, and within a solid angle $\mathrm{d}\Omega$, is given for a Stokes process by [15]

$$\frac{\mathrm{d}^2 S}{\mathrm{d}\Omega\, \mathrm{d}\omega_d} = \frac{\omega_d^4}{16\pi^2 c^4}[B(\omega) + 1]\hbar \sum_{i,j,k,l} v_i v_k I_{ijkl}(\omega) w_j w_l, \quad (4)$$

where $\omega = \omega_0 - \omega_d$ and

$$I_{ijkl}(\omega) = \sum_m a^\star_{ij}(m) a_{kl}(m) \frac{1}{2\omega_m}[\delta(\omega - \omega_m) - \delta(\omega + \omega_m)]. \quad (5)$$

In these equations, (i, j, k, l) indices denote the Cartesian components, the asterisk symbolizes the complex conjugation, c is the speed of light in the medium, $\hbar$ is the reduced Planck constant, ω_0 (resp. ω_d) is the frequency of incident (resp. scattered) light, $\mathbf{v}$ (resp. $\mathbf{w}$) is the polarization unit vector of the incident (resp. scattered) light, and $B(\omega)$ is the Bose factor. The Raman susceptibility tensor is defined as

$$a_{ij}(m) = \sqrt{\Omega_0} \sum_{\kappa,\gamma} \pi^\kappa_{ij,\gamma} U_m(\gamma\kappa), \quad (6)$$

where the sum runs over all atoms κ and space directions γ, Ω_0 is the unit cell volume and $\tilde{\pi}$ is a third-rank tensor describing the changes of the linear dielectric susceptibility induced by an individual atomic displacement defined as

$$\pi^\kappa_{ij,\gamma} = \left.\frac{\partial \chi^{(1)}_{ij}}{\partial \tau_{\kappa\gamma}}\right|_0, \quad (7)$$

where $\tau_{\kappa\gamma}$ corresponds to the displacement of the κth atom in the direction γ.

For TO phonons ($\boldsymbol{\mathcal{E}} = \mathbf{0}$, where $\boldsymbol{\mathcal{E}}$ is the electric field), $\tilde{\pi}$ can be computed as a mixed third-order derivative of the energy functional, $\mathcal{F}$, with respect to an electric field, twice, and to an atomic displacement under the condition of zero electric field [11]:

$$\pi^\kappa_{ij,\gamma}\big|_{\mathcal{E}=0} = -\frac{6}{\Omega_0} \mathcal{F}^{\tau_{\kappa\gamma}\mathcal{E}_i\mathcal{E}_j}. \quad (8)$$

For the case of LO phonons ($\boldsymbol{\mathcal{D}} = \mathbf{0}$, where $\boldsymbol{\mathcal{D}}$ is the electric displacement vector) with wavevector $\mathbf{q} \to \mathbf{0}$ in a polar crystal, equation (6) must additionally take into account the effect of the macroscopic electric field generated by the lattice polar vibration. This field enters into the computation of the Raman susceptibilities at two levels. On the one hand, it gives rise to the non-analytical part of the dynamical matrix that modifies the frequencies and eigenvectors with respect to pure TO phonons. On the other hand, the electric field induces an additional change in the dielectric susceptibility tensor related to the nonlinear optical coefficients $\chi^{(2)}_{ijk}$. Thus, for LO phonons, equation (8) has to be modified as follows [16]:

$$\pi^\kappa_{ij,\gamma}\big|_{\mathcal{D}=0} = \pi^\kappa_{ij,\gamma}\big|_{\mathcal{E}=0} - \frac{8\pi}{\Omega_0} \frac{\sum_l Z^*_{\gamma l}(\kappa) q_l}{\sum_{l,l'} q_l \varepsilon^\infty_{ll'} q_{l'}} \sum_l \chi^{(2)}_{ijl} q_l. \quad (9)$$

Thus, the Raman calculation requires several ingredients, such as the vibrational frequencies and eigenmodes obtained

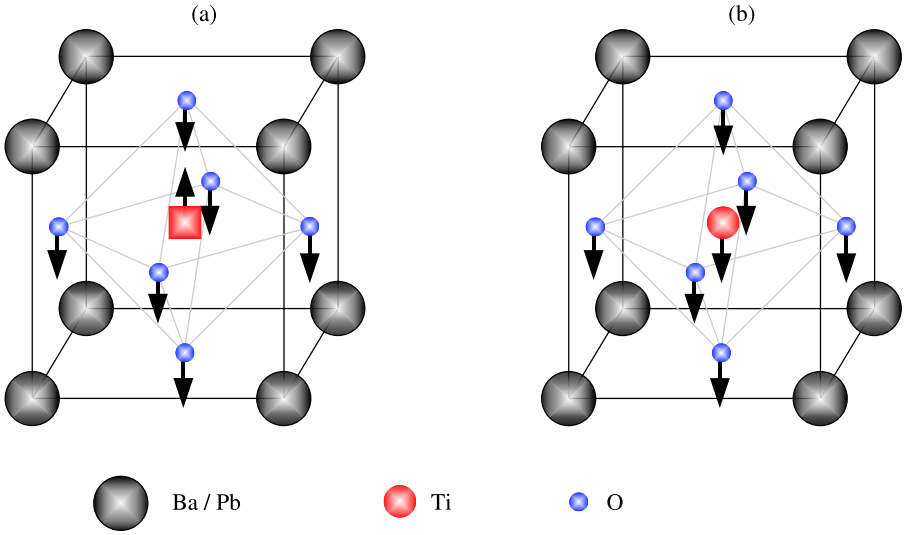

Figure 1. Atomic displacements at the transition from the cubic to the tetragonal phase of $BaTiO_3$ (a) and $PbTiO_3$ (b). Arrows indicate the direction of the atomic displacements taking place at the phase transition when the A-atoms are chosen as reference. Amplitudes of the displacements are reported in table 2.

(This figure is in colour only in the electronic version)

from the diagonalization of D, as well as the Z^*, ε^∞, $\chi^{(2)}$ and π tensors. All these quantities should be in relative good agreement with the experimental ones to have a reliable prediction on the Raman spectra. In the next sections, all these quantities will be computed, discussed and confronted with the experimental results, when available.

3. Computational details

First-principles calculations were performed within the local density approximation (LDA) to density functional theory as implemented in the ABINIT package [17]. We used highly transferable Teter pseudopotentials [18]. Ba ($5s^2$, $5p^6$, $6s^2$), Pb ($5d^{10}$, $6s^2$, $6p^2$), Ti ($3s^2$, $3p^6$, $3d^2$, $4s^2$) and O ($2s^2$, $2p^4$) electrons were treated as valence states in the construction of the pseudopotentials. The self-consistent cycles converged within a tolerance of 10^{-15} Ha on the potential residual. The wavefunction was expanded in plane waves up to a kinetic energy cutoff of 55 Ha. Integrals over the Brillouin zone were replaced by sums over a $10 \times 10 \times 10$ mesh of special k-points according to the Monkhorst–Pack scheme [19]. Both this energy cutoff and k-point mesh were sufficient to reach convergence of all the quantities required for a Raman calculation. The dynamical matrix (yielding phonon frequencies and eigendisplacements), as well as the Z^* and ε^∞ tensors, were computed within a variational approach to density functional perturbation theory.

4. Structures

At high enough temperatures, both $BaTiO_3$ and $PbTiO_3$ crystallize in the centrosymmetric cubic perovskite structure of $Pm\bar{3}m$ symmetry and five atoms per unit cell (see figure 1). As the temperature is lowered, $BaTiO_3$ undergoes a sequence of three ferroelectric phase transitions. Around 403 K, it transforms to a tetragonal structure ($P4mm$) with a spontaneous polarization along the $\langle 100 \rangle$ direction, as shown in figure 1(a). This phase is stable until about 278 K where there is a transformation to a phase of orthorhombic symmetry ($Pmm2$) with a spontaneous polarization along the $\langle 110 \rangle$ direction. The last phase transition arises around 183 K. The low-temperature structure of $BaTiO_3$ is rhombohedral ($P3m1$) and the polarization of this phase is aligned along the $\langle 111 \rangle$ direction. In contrast to $BaTiO_3$, $PbTiO_3$ undergoes a unique phase transition around 763 K to a tetragonal $P4mm$ phase (see figure 1(b)).

In the following, the $BaTiO_3$ and $PbTiO_3$ tetragonal phase will be first studied. The comparison of these phases will allow us to investigate the effects of the substitution of Ba atoms by Pb atoms on their Raman spectra. Then, the case of the $BaTiO_3$ rhombohedral ferroelectric phase will be investigated because: (i) it is the phase thermodynamically stable of $BaTiO_3$, (ii) a few experimental Raman studies are devoted to this phase [12, 13] mainly due to its low-temperature structure and (iii) only one theoretical article is reported in the literature about its phonon investigations [20].

For all three ferroelectric structures, we worked at the experimental lattice parameters, which usually lead to a better comparison with experimental data at finite temperature. Internal atomic position relaxations were performed using the Broyden–Fletcher–Goldfarb–Shanno algorithm [21] until the maximum residual force on the atoms was less than 6×10^{-6} Ha/bohr. The atomic positions of these ferroelectric phases are reported in table 1. The Ba atom has been chosen as the reference and remains located at the origin. In each phase, the Ti atom is slightly displaced from its central position, along the polar axis. Due to symmetry, two oxygen atoms are equivalent in the tetragonal phases (O_2 and O_3) while all the oxygens are equivalent in the rhombohedral phase. Results

Table 1. Atomic positions (in reduced coordinates) of the $BaTiO_3$ and $PbTiO_3$ tetragonal phase and $BaTiO_3$ rhombohedral phase.

Atom	Tetragonal	Rhombohedral
Ba/Pb	(0, 0, 0)	(0, 0, 0)
Ti	$(\frac{1}{2}, \frac{1}{2}, \frac{1}{2} + \delta_{Ti})$	$(\frac{1}{2} + \delta_{Ti}, \frac{1}{2} + \delta_{Ti}, \frac{1}{2} + \delta_{Ti})$
O_1	$(\frac{1}{2}, \frac{1}{2}, 0 + \delta_{O_1})$	$(\frac{1}{2} + \delta_{O_1}, \frac{1}{2} + \delta_{O_1}, \delta_{O_2})$
O_2	$(\frac{1}{2}, 0, \frac{1}{2} + \delta_{O_2})$	$(\frac{1}{2} + \delta_{O_1}, \delta_{O_2}, \frac{1}{2} + \delta_{O_2})$
O_3	$(0, \frac{1}{2}, \frac{1}{2} + \delta_{O_2})$	$(\delta_{O_2}, \frac{1}{2} + \delta_{O_1}, \frac{1}{2} + \delta_{O_1})$

Table 2. Calculated ferroelectric displacements of the $BaTiO_3$ and $PbTiO_3$ tetragonal phase and $BaTiO_3$ rhombohedral phase at experimental lattice parameters (see notations in table 1), together with the experimental ones. Lattice parameters are in Å, the rhombohedral angle (α_{rh}) is in degrees and the displacements are in reduced coordinates.

	$BaTiO_3$				$PbTiO_3$	
	Rhombohedral		Tetragonal			
	Present	Exp. [32]	Present	Exp. [32]	Present	Exp. [33]
a (a_{rh})	(4.003)		3.994		3.904	
c (α_{rh})	(89.84)		4.036		4.152	
δ_{Ti}	−0.0105	−0.011	0.0136	0.0215	−0.0478	−0.040
δ_{O_1}	0.0116	0.0129	−0.0273	−0.0233	−0.1205	−0.112
δ_{O_2}	0.0183	0.0191	−0.0167	−0.0100	−0.1278	−0.112

of the relaxations giving the ferroelectric displacements with respect to the paraelectric phases are reported in table 2, where they are compared to experimental ones. The three sets of data are found to be in excellent agreement both for the amplitude of the ferroelectric displacements and their directions.

5. Nonlinear optical susceptibility tensor

The second-order nonlinear optical susceptibility, $\chi^{(2)}$, is a third-rank tensor related to the electronic response of the system and which depends on the frequencies of the optical electrical fields [22]. However, in the present context of the $2n + 1$ theorem applied within the LDA to (static) DFT, we neglect the dispersion of $\chi^{(2)}$ computing the electronic response at zero frequency. Within these conditions, the $\chi^{(2)}$ tensor is related to a third-order derivative of a field-dependent energy functional, $\mathcal{F} = E - \Omega_0 \boldsymbol{\mathcal{E}} \cdot \boldsymbol{\mathcal{P}}$, where E, $\boldsymbol{\mathcal{E}}$ and $\boldsymbol{\mathcal{P}}$ are, respectively, the total energy in zero field, the macroscopic electric field and the macroscopic polarization [11]. As a consequence, the $\chi^{(2)}$ tensor satisfies Kleinman's symmetry condition [23] and its indices are therefore symmetric under a permutation. In the following, and as usual in nonlinear optics, we will report, instead of $\chi^{(2)}$, the d tensor defined as $d = \frac{1}{2}\chi^{(2)}$.

In the $BaTiO_3$ and $PbTiO_3$ tetragonal phase, the d tensor has three independent elements and can be written as

$$d_{ij} = \begin{pmatrix} 0 & 0 & 0 & 0 & d_{15} & 0 \\ 0 & 0 & 0 & d_{15} & 0 & 0 \\ d_{31} & d_{31} & d_{33} & 0 & 0 & 0 \end{pmatrix}, \qquad (10)$$

Table 3. Calculated and experimental independent elements of the nonlinear optical susceptibility tensor (in pm V^{-1}) and electronic dielectric tensor of ferroelectric $BaTiO_3$ and $PbTiO_3$ in their tetragonal phase, and $BaTiO_3$ in its rhombohedral phase. Experimental data are from [34–38] for $BaTiO_3$ and from [31, 39, 40] for $PbTiO_3$.

	$BaTiO_3$			$PbTiO_3$	
	Rhombohedral	Tetragonal			
	Present	Present	Exp.	Present	Exp.
d_{15}	10.97	−11.09	−17.0	−27.69	−37.9
d_{31}	10.97	−11.09	−15.7	−27.69	−42.8
d_{33}	24.69	−18.31	−6.8	−5.69	+8.5
d_{22}	−0.98				
ϵ^{∞}_{xx}	6.16	6.48	5.19	7.31	6.64
ϵ^{∞}_{zz}	5.73	5.84	5.05	6.79	6.63

where the indices i and j denote the Cartesian components in Voigt notation.

In the $BaTiO_3$ rhombohedral phase, this tensor has one additional independent element, d_{22}, due to the lower symmetry of this phase. Thus, the form of this tensor becomes

$$d_{ij} = \begin{pmatrix} 0 & 0 & 0 & 0 & d_{15} & -d_{22} \\ -d_{22} & d_{22} & 0 & d_{15} & 0 & 0 \\ d_{31} & d_{31} & d_{33} & 0 & 0 & 0 \end{pmatrix}. \qquad (11)$$

Kleinman's symmetry rule allows us to reduce these tensors to, respectively, two and three independent elements since in this case we have $d_{31} = d_{15}$. The calculated independent elements of the d tensor in the $BaTiO_3$ and $PbTiO_3$ tetragonal phase and in the $BaTiO_3$ rhombohedral phase are given in table 3, together with the experimental values only available for the tetragonal phases. These calculated tensorial elements are reported for the first time for these three ferroelectric phases to the best of our knowledge. The calculated absolute values of the nonlinear optical susceptibilities are in reasonable agreement with the corresponding experimental values. All calculated susceptibilities are found to be negative for the tetragonal phases. In the case of $BaTiO_3$, these results correspond to the experimental observations. Nevertheless, a positive value has been experimentally reported for d_{33} in $PbTiO_3$. Nonlinear optical susceptibilities are particularly difficult to measure accurately and the values reported by different authors are often in substantial disagreement [24]. Thus, as the sign is unambiguously defined in our calculations, we suggest that the positive sign of d_{33} reported experimentally might result from a wrong interpretation of the experimental measurements.

6. Dielectric and Born effective charge tensors

Born effective charge (Z^*) and optical dielectric tensor (ϵ^{∞}) describe the strength of the coupling between the lattice displacements and electrostatic fields in a polar insulator. In particular, these quantities are essential to investigate ferroelectric materials where phase transitions take place from the competition of long-range Coulomb interactions and short-range forces [20]. Applying a linear response approach,

Table 4. Born effective charge tensors ($Z^*_{\alpha\beta}(\kappa)$) in the tetragonal and rhombohedral phases of $BaTiO_3$ and in the $PbTiO_3$ tetragonal phase (in $|e|$).

	$BaTiO_3$		$PbTiO_3$
κ	Rhombohedral	Tetragonal	Tetragonal
Ba/Pb	$\begin{pmatrix} 2.783 & & \\ & 2.783 & \\ & & 2.737 \end{pmatrix}$	$\begin{pmatrix} 2.726 & & \\ & 2.726 & \\ & & 2.814 \end{pmatrix}$	$\begin{pmatrix} 3.730 & & \\ & 3.730 & \\ & & 3.339 \end{pmatrix}$
Ti	$\begin{pmatrix} 6.608 & & \\ & 6.608 & \\ & & 5.765 \end{pmatrix}$	$\begin{pmatrix} 7.044 & & \\ & 7.044 & \\ & & 5.971 \end{pmatrix}$	$\begin{pmatrix} 6.090 & & \\ & 6.090 & \\ & & 5.327 \end{pmatrix}$
O_1	$\begin{pmatrix} -2.562 & -0.984 & 0.647 \\ -0.984 & -3.699 & 1.121 \\ 0.733 & 1.269 & -2.834 \end{pmatrix}$	$\begin{pmatrix} -2.024 & & \\ & -2.024 & \\ & & -4.836 \end{pmatrix}$	$\begin{pmatrix} -2.066 & & \\ & -2.066 & \\ & & -4.499 \end{pmatrix}$
O_2		$\begin{pmatrix} -2.149 & & \\ & -5.596 & \\ & & -1.974 \end{pmatrix}$	$\begin{pmatrix} -2.684 & & \\ & -5.070 & \\ & & -2.083 \end{pmatrix}$

we have calculated Z^* and ϵ^∞ in the $BaTiO_3$ and $PbTiO_3$ tetragonal phase and in the $BaTiO_3$ rhombohedral phase. Our calculated tensorial components of Z^* related to the asymmetric unit of these three ferroelectric phases are reported in table 4 and are in agreement with previous density functional calculations [25].

As usual in the class of ABO_3 materials, the amplitude of some tensorial elements of Z^* significantly deviates from their nominal value expected in a purely ionic picture. In addition, we observe that the anomalous effective charges on Ba or Pb atoms are smaller than the anomalous effective charges on Ti or O atoms, when considering a displacement of the latter along Ti–O bonds. The amplitude of Z^* in these materials can be explained from their electronic structure as interpreted within the Harrison bond orbital model [26]: the Ba atom in $BaTiO_3$ and, to a much lower extent, the Pb atom in $PbTiO_3$ are close to a fully ionized configuration whereas there is a partly covalent interaction between Ti and O. During an atomic displacement, the parameters that determine the covalent interactions between Ti 3d and O 2p atomic orbitals (the hopping integrals) vary. Thus, this variation produces a dynamical charge transfer between Ti and O atoms, which is at the origin of the anomalous effective charges of these atoms.

The calculated ϵ^∞ in the $BaTiO_3$ and $PbTiO_3$ tetragonal phase and in the $BaTiO_3$ rhombohedral phase are reported in table 3 where they are compared to the available experimental data. Due to the symmetry of these three ferroelectric phases, ϵ^∞ is diagonal and assumes different values for parallel and perpendicular directions to the optical axis (z axis). We observe a significant overestimate of the calculated tensorial elements of ϵ^∞ with respect to the experimental ones, as usual in DFT. This problem has been previously discussed in the literature [27, 28] and has been related to the lack of polarization dependence of local (LDA) and quasi-local (GGA) exchange–correlation functionals. In spite of this error on the absolute value, the evolutions of ϵ^∞ are, in general, qualitatively well described by LDA or GGA calculations. We observe that ϵ^∞ is always lower along the polar axis, as is also the case for Z^*. No experimental data was reported for the rhombohedral phase.

7. Vibrational properties

The zone-center optical phonon modes of the $BaTiO_3$ and $PbTiO_3$ tetragonal phase can be respectively classified, according to their irreducible representations, into $4A_1 \oplus B_1 \oplus 5E$. The irreducible representation of the $BaTiO_3$ rhombohedral phase is exactly the same except for the B_1 mode which must be replaced by an A_2 mode. One A_1 mode and one E mode are uniform translational modes. The A_1 and E modes are both Raman-and infrared-active, the B_1 mode is only Raman-active and the A_2 mode is silent. The nondegenerate A_1 modes are polarized along the optical axis, whereas the doubly degenerate E modes are perpendicularly polarized to this axis.

At the Γ point, the macroscopic electric field splits the infrared active modes into TO and LO modes. The LO–TO splitting of the E modes occurs for $\mathbf{q}$ vectors orthogonal to the z axis, while the E modes remain degenerate at the E(TO) frequencies for $\mathbf{q}$ parallel to the z axis. Similarly, the frequencies for A_1(TO) and A_1(LO) modes are obtained by diagonalizing the full dynamical matrix with $\mathbf{q}$ orthogonal and parallel to the z axis, respectively.

Tables 5 and 6, respectively, report our calculated phonon frequencies and eigendisplacement vectors of the $BaTiO_3$ and $PbTiO_3$ tetragonal phase. Our calculated phonon frequencies of the $BaTiO_3$ rhombohedral phase are also reported in table 5 with, to the best of our knowledge, the only one density functional calculation provided in the literature. No experimental phonon of this phase recorded from a monocrystal exists in the literature. Our computed frequencies have been obtained from the equilibrium geometry at the experimental lattice parameters. We observe that our theoretical frequencies are close to those reported experimentally and theoretically in the literature, with relative errors generally smaller than 10%. The differences between the theoretical approaches are attributed to the different equilibrium structures related to the different unit cell volume used.

Table 5. Calculated and experimental frequencies (in cm^{-1}) of the TO and LO phonon modes of the $BaTiO_3$ and $PbTiO_3$ tetragonal phase and $BaTiO_3$ rhombohedral phase. Experimental data obtained by Raman spectroscopy when available.

		$BaTiO_3$					$PbTiO_3$		
		Rhombohedral		Tetragonal					
		Present	Calc.[a] [20]	Present	Exp. [41]	Exp. [30]	Present	Exp. [30]	Exp. [31]
A_1	TO1	167	168	161	178	176	151	148	149
	LO1	178	180	180	189		189		194
	TO2	259	265	302	276	275	357	362	359
	LO2	461	462	452	471	471	442		465
	TO3	512	505	507	515	518	653	650	647
	LO3	676	702	705	725	720	791		795
E	TO1	163	161	161*i*	38		78	89	87
	LO1	174	173	162	180	179	117	130	128
	TO2	210	205	167	180	179	199	220	219
	LO2	293	293	284	308	308	269	290	289
	TO3	293	293	284	308	307	269	290	289
	LO3	441	438	444	466	467	416	440	441
	TO4	470	461	457	498	488	482	508	505
	LO4	687	725	641	722	708	655	720	687
B_1/A_2		277	274	287	304	303	283		289

[a] Calculation performed at optimized lattice parameters.

Table 6. Calculated eigendisplacement vectors **U** (in bohr) of the TO phonon modes of the $BaTiO_3$ and $PbTiO_3$ tetragonal phase according to the normalization convention defined in equation (3) (masses in au). E and A_1 modes are respectively polarized along the x and z axes. The labels of the atoms and modes correspond to those defined in tables 1 and 5, respectively.

	$BaTiO_3$					$PbTiO_3$				
	Ba	Ti	O_1	O_2	O_3	Pb	Ti	O_1	O_2	O_3
E(TO1)	0.0020	0.0963	−0.0721	−0.0831	−0.1503	0.0377	−0.0557	−0.1222	−0.1073	−0.0916
E(TO2)	0.0546	−0.0812	−0.0773	−0.0816	−0.0672	0.0094	−0.1168	0.0445	0.1222	0.0602
E(TO3)	0.0007	0.0026	−0.1829	0.1703	−0.0012	0.0040	−0.0276	0.1973	−0.1432	−0.0237
E(TO4)	0.0018	−0.0269	0.1165	0.1251	−0.1764	0.0015	0.0094	0.0578	0.1106	−0.2159
A_1(TO1)	0.0544	−0.0667	−0.0833	−0.0918	−0.0918	0.0389	−0.0760	−0.0949	−0.0910	−0.0910
A_1(TO2)	0.0061	−0.1097	0.0699	0.1031	0.1031	0.0024	−0.0921	−0.0253	0.1349	0.1349
A_1(TO3)	0.0008	0.0101	−0.2154	0.0889	0.0889	0.0021	−0.0577	0.2226	−0.0383	−0.0383

8. π tensors

In the $BaTiO_3$ and $PbTiO_3$ tetragonal phase, the π tensors take a very simple form due to the high symmetry position of the atoms in these structures, as shown in table 7. For each atom in the unit cell, these tensorial elements are determined by five numbers denoted a, b, c, d and e, and in the case of Ba, Pb, Ti and O_1 atoms, the number of these independent elements is even smaller because $a = b$ and $c = d$. In contrast, due to the lower symmetry position of the atoms in the $BaTiO_3$ rhombohedral phase, the π tensors do not have a simple form and have six independent elements to be calculated for Ba and Ti atoms, and eighteen for O_1 atoms.

Table 8 reports the independent elements of the π tensor for the TO phonon modes of $BaTiO_3$ and $PbTiO_3$ in their tetragonal phase, whereas those associated with the $BaTiO_3$ rhombohedral phase are reported in table 9. Only the atoms constituting the asymmetric unit of these three ferroelectric phases have been reported. π tensors for the other atoms of the unit cell can be determined by symmetry operations. We observe that the absolute values of the π elements for Ba and Pb atoms are significantly smaller than their corresponding values for the Ti or O atoms when considering a displacement of the latter along Ti–O bonds. A similar behavior has been observed and discussed for Z^* in section 6. Thus, our calculations point out that atoms with a giant Z^* are also those which exhibit the largest π.

Table 7. $\pi^{\kappa}_{ij,\gamma}$ tensor symmetry of Ba, Pb, Ti and O atoms in the $BaTiO_3$ and $PbTiO_3$ tetragonal phase. x, y and z denote the direction of the atomic displacement, γ. The rows and columns of the matrices correspond to the indexes i and j.

x	y	z
$\begin{pmatrix} \cdot & \cdot & a \\ \cdot & \cdot & \cdot \\ a & \cdot & \cdot \end{pmatrix}$	$\begin{pmatrix} \cdot & \cdot & \cdot \\ \cdot & \cdot & b \\ \cdot & b & \cdot \end{pmatrix}$	$\begin{pmatrix} c & \cdot & \cdot \\ \cdot & d & \cdot \\ \cdot & \cdot & e \end{pmatrix}$

In order to clarify this correlation, we can remember that the derivatives of the linear optical susceptibility with respect to an atomic displacement can be alternatively expressed as derivatives of Z^* with respect to an electric field:

$$\pi^{\kappa}_{ij,\gamma} = \frac{\partial \chi^{(1)}_{ij}}{\partial \tau_{\kappa\gamma}} = \frac{1}{\Omega_0} \frac{\partial Z^*_{\gamma j}(\kappa)}{\partial \mathcal{E}_i}. \quad (12)$$

In this class of materials, the anomalous Z^* arises from

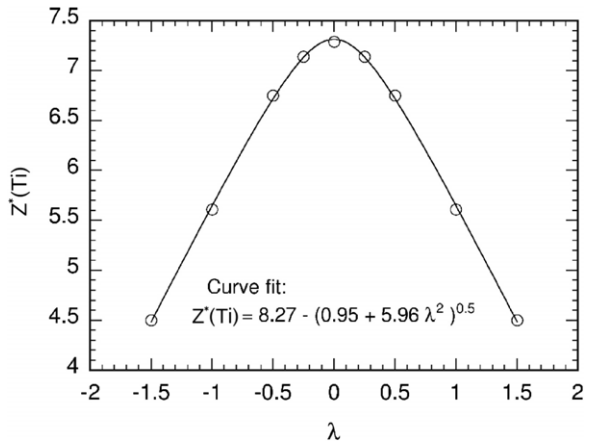

Figure 2. Evolution of the amplitude of Z^*(Ti) in the ⟨111⟩ direction (in $|e|$) from the cubic ($\lambda = 0$) to the rhombohedral ($\lambda = 1$) phase. The distortion of the cubic unit cell has been neglected.

Table 8. Independent elements of $\pi^{\kappa}_{ij,\gamma}$ tensor (in bohr^{-1}) related to the asymmetric unit of the $BaTiO_3$ and $PbTiO_3$ in their tetragonal phase for TO modes (see notations in table 7).

κ		$BaTiO_3$	$PbTiO_3$
Ba/Pb	a, b	−0.0039	−0.0265
	c, d	−0.0065	−0.0826
	e	0.0218	−0.0485
Ti	a, b	−0.0873	−0.1405
	c, d	−0.1288	−0.1561
	e	−0.3093	−0.1276
O_1	a, b	0.0335	0.0620
	c, d	0.1206	0.1924
	e	0.2462	0.1783
O_2	a	−0.0030	−0.0240
	b	0.0606	0.1289
	c	−0.0063	−0.0362
	d	0.0210	0.0825
	e	0.0207	−0.0011

the fact that the O 2p and Ti 3d orbital hybridization is strongly sensitive to atomic displacements [25, 26]. It is worth noticing that this effect is strongly nonlinear and that Z^* is strongly sensitive to atomic displacement: as a general rule in ABO_3 compounds, Z^* is significantly less anomalous in the low symmetry phase than in the cubic perovskite reference structure (see figure 2). The present study shows that anomalous Z^* are not only sensitive to perturbations like atomic displacements, but also to other types of perturbation such as an electric field. In addition, the amplitude of the π elements depends on the way the dynamical charge transfer is affected by an electric field. In the case of Ba and Pb atoms, the charge transfer is close to zero and, because of the ionic configuration of these atoms, it is only slightly affected by an electric field. By contrast, because of the partly covalent interactions between Ti and O atoms, the charge transfer between these atoms is more sensitive to an electric field. The amplitude of the π elements can therefore be interpreted from similar arguments as the amplitude of Z^*, and both Z^* and π will scale similarly.

9. Raman spectra of prototypical ferroelectrics

Now, we have computed all the quantities required for the calculation of the Raman spectra of $BaTiO_3$ and $PbTiO_3$ in their tetragonal phases and $BaTiO_3$ in its rhombohedral phase. These quantities have been compared to the available experimental ones and are found to be in relatively good agreement. So, we can expect a reliable prediction of the calculated Raman spectra of these materials.

As discussed in section 2.2, the Raman scattering efficiencies can be computed from the projection of the Raman susceptibility tensors, $a_{ij}(m)$, on the polarization vectors of the incoming and scattered photons (equation (4)). The form of these Raman tensors depends on the crystal symmetry. Following Loudon's notation [29], the Raman susceptibility tensors of the A_1 and B_1 modes are given by

$$A_1(z) = \begin{pmatrix} a & \cdot & \cdot \\ \cdot & a & \cdot \\ \cdot & \cdot & b \end{pmatrix}, \qquad \text{and} \qquad B_1 = \begin{pmatrix} c & \cdot & \cdot \\ \cdot & -c & \cdot \\ \cdot & \cdot & \cdot \end{pmatrix}. \tag{13}$$

In contrast, the Raman tensors of the E modes are different between the tetragonal and rhombohedral phases. For the $BaTiO_3$ and $PbTiO_3$ tetragonal phase, and in the case of the modes which are polarized along x or y, the Raman susceptibility tensors can be expressed as

$$E(x) = \begin{pmatrix} \cdot & \cdot & e \\ \cdot & \cdot & \cdot \\ e & \cdot & \cdot \end{pmatrix}, \qquad E(y) = \begin{pmatrix} \cdot & \cdot & \cdot \\ \cdot & \cdot & e \\ \cdot & e & \cdot \end{pmatrix}, \tag{14}$$

whereas for the $BaTiO_3$ rhombohedral phase, these tensors become

$$E(x) = \begin{pmatrix} \cdot & e & f \\ e & \cdot & \cdot \\ f & \cdot & \cdot \end{pmatrix}, \qquad E(y) = \begin{pmatrix} e & \cdot & \cdot \\ \cdot & -e & f \\ \cdot & f & \cdot \end{pmatrix}. \tag{15}$$

The method presented in section 2.2 to compute the Raman spectra gives no information about the shape or the width of the Raman lines mainly because the electron–phonon coupling is not taken into account within the formalism used. Thus, for all the calculated Raman spectra shown in the following, the Raman lineshape is assumed to be Lorentzian and the linewidth is fixed at 4 cm^{-1}. Note that the experimental data are generally obtained at room temperature, whereas the theoretical results account for the temperature only through the statistical Bose factor.

9.1. Raman spectra of the $PbTiO_3$ tetragonal phase

Figure 3 compares the calculated Raman spectra of the $PbTiO_3$ tetragonal phase and the experimental ones obtained for two scattering configurations. The bottom spectra have been obtained for an $x(zz)y$ scattering configuration in which the incoming photon has its wavevector along x and its polarization along z while the scattered photon has its wavevector along y and its polarization along z. Thus, only pure A_1(TO) modes can be detected in this configuration. The spectra at the top of figure 3 have been obtained for an $x(zx)y$ configuration where the wavevector and polarization of the

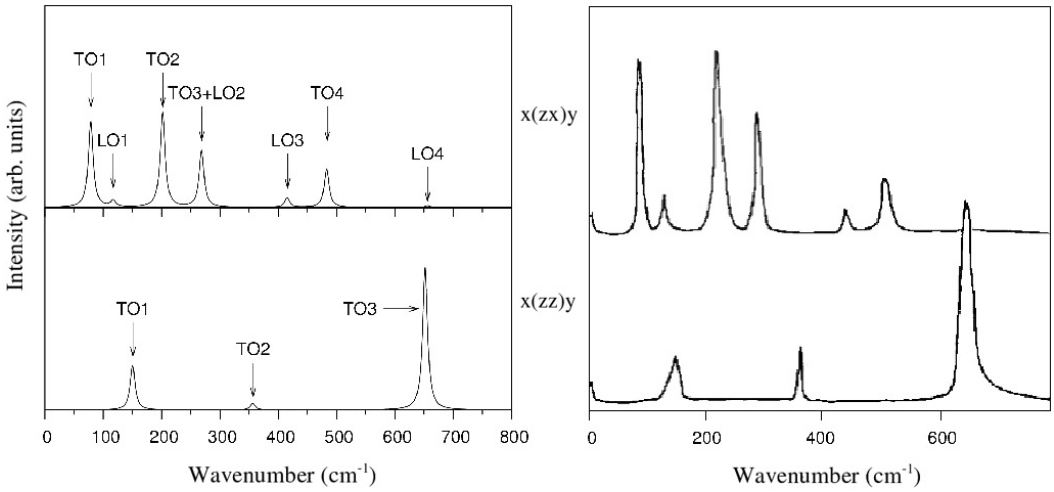

Figure 3. Theoretical (left) and experimental [30] (right) Raman spectra of $PbTiO_3$ tetragonal phase. The top and the bottom spectra have been obtained for an $x(zx)y$ and $x(zz)y$ scattering configuration, respectively. In these configurations, only the E(TO) + E(LO) and A_1(TO) modes can be detected, respectively. The experimental spectra are recorded at room temperature.

Table 9. $\pi^{\kappa}_{ij,\gamma}$ tensor elements of the TO modes ($\times 10^{-3}$ Bohr^{-1}) related to the asymmetric unit of the $BaTiO_3$ rhombohedral phase.

	γ		
κ	x	y	z
Ba	$\begin{pmatrix} -10.8 & & -9.9 \\ & 10.8 & \\ -9.9 & & \end{pmatrix}$	$\begin{pmatrix} & 10.8 & \\ 10.8 & & -9.9 \\ & -9.9 & \end{pmatrix}$	$\begin{pmatrix} -10.2 & & \\ & -10.2 & \\ & & -0.1 \end{pmatrix}$
Ti	$\begin{pmatrix} 44.9 & & 145.5 \\ & -44.9 & \\ 145.5 & & \end{pmatrix}$	$\begin{pmatrix} & -44.9 & \\ -44.9 & & 145.5 \\ & 145.5 & \end{pmatrix}$	$\begin{pmatrix} 188.4 & & \\ & 188.4 & \\ & & 315.3 \end{pmatrix}$
O_1	$\begin{pmatrix} 36.5 & 16.1 & -36.0 \\ 16.1 & 40.64 & -15.9 \\ -36.0 & -15.9 & 52.1 \end{pmatrix}$	$\begin{pmatrix} 50.6 & 20.7 & -15.9 \\ 20.7 & 82.9 & -54.4 \\ -15.9 & -54.4 & 90.3 \end{pmatrix}$	$\begin{pmatrix} -57.4 & -3.5 & 28.9 \\ -3.5 & -61.4 & 50.1 \\ 28.9 & 50.1 & -105.1 \end{pmatrix}$

incoming photon (scattered photon) are along x and z (y and x), respectively. Thus, both E(TO) and E(LO) modes can be detected in this configuration.

As expected, these figures show a relatively good agreement between the calculated and experimental spectra of the $PbTiO_3$ tetragonal phase for both the position of the Raman lines and their intensities. In the case of the E modes, the LO4 line predicted at 655 cm^{-1} has the weakest scattering efficiency. However, it does not even appear on the experimental spectrum although it is reported in [30] to be around this frequency.

9.2. Raman spectra of the $BaTiO_3$ tetragonal phase

Figure 4 compares the calculated Raman spectra of the $BaTiO_3$ tetragonal phase and the experimental ones obtained for $y(zz)\bar{y}$ and $z(yz)x$ scattering configurations. In these configurations, only the A_1(TO) and E(TO) modes can be detected, respectively. As in the case of the $PbTiO_3$ tetragonal phase, these figures show a very good agreement between the calculated and experimental spectra for both the frequency position of the Raman lines and their intensities.

In the case of the A_1 modes, the TO2 and TO3 lines are correctly predicted both in position and relative intensity, and also have the strongest scattering efficiency. The TO1 line appears weaker on the calculated spectrum than on the experimental one. However, this effect is not related to the intrinsic scattering efficiency of the TO1 mode. It is rather a consequence of the fact that the TO2 line in the experimental spectrum is quite broad and that it overlaps with the TO1 line, whereas this is not the case for the calculated spectrum since we use a constant linewidth to represent the Raman lines.

In the case of the E modes, only the assignment of three Raman E(TO) modes remains possible since one E mode is unstable in the harmonic approximation. These three Raman lines are correctly predicted both in frequency position and relative intensity. The calculated TO3 line dominates the spectrum while the intensity of the calculated TO2 line is weaker than that of the other Raman lines, in agreement with the experimental data.

9.3. Raman spectra of the $BaTiO_3$ rhombohedral phase

Finally, we have also computed the Raman spectra of the $BaTiO_3$ rhombohedral phase since only a few theoretical [20] or experimental [12, 13] studies were devoted to this phase. Figure 5 displays the calculated Raman intensities of the A_1(TO) and E(TO) modes of the $BaTiO_3$ rhombohedral phase

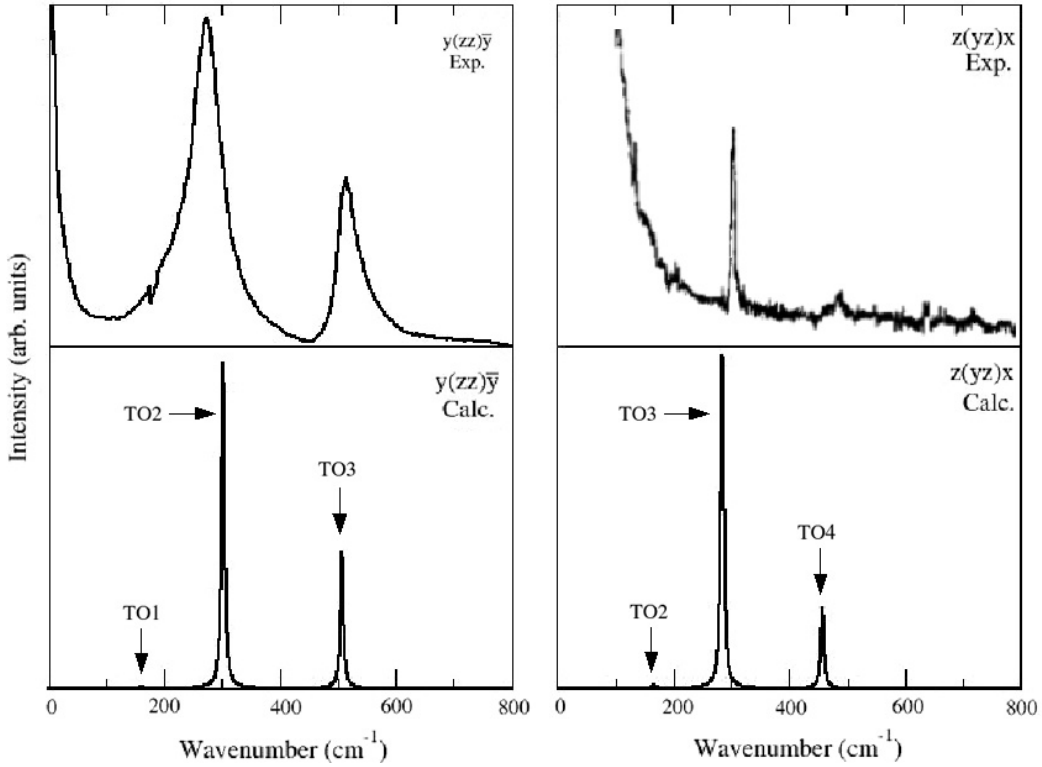

Figure 4. Theoretical (bottom) and experimental (top) Raman spectra of the $BaTiO_3$ tetragonal phase for $y(zz)\bar{y}$ and $z(yz)x$ scattering configurations. In these configurations, only the A_1(TO) and E(TO) modes can be detected, respectively. The experimental spectra in the $y(zz)\bar{y}$ and $z(yz)x$ configurations are respectively from [42] and [12], and are recorded at room temperature.

for the $x(zz)y$ and $z(xy)\bar{z}$ configurations, respectively. To the best of our knowledge, there is no Raman spectrum of this phase on the monocrystal in the literature. This study therefore provides benchmark results for future interpretation of experimental data. We observe that the Raman relative intensity and frequency position of the A_1(TO) lines of the $BaTiO_3$ rhombohedral phase are very close to those observed and calculated for its tetragonal phase. Similarly, the frequency position and relative intensity of the E(TO1), E(TO2) and E(TO4) lines show the same agreement. Nevertheless, the E(TO3) line predicted at 293 cm^{-1}, absent in the $BaTiO_3$ tetragonal phase, is a Raman fingerprint of the rhombohedral phase.

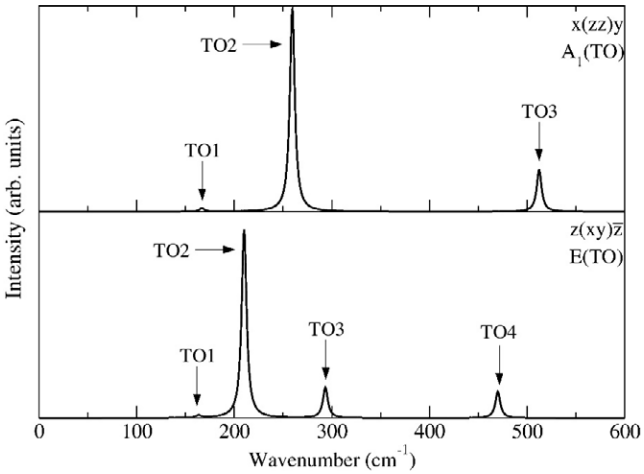

Figure 5. Theoretical Raman spectra of the $BaTiO_3$ rhombohedral phase for $x(zz)y$ and $z(xy)\bar{z}$ scattering configurations. In these configurations, only the A_1(TO) and E(TO) modes can be detected, respectively.

10. Discussion

It is usual to use the atomic polarizability concept when modeling the dielectric susceptibility. Within this concept, the dielectric susceptibility of a crystal is decomposed into individual atomic polarizability contributions. It can therefore be questioned whether the Raman susceptibility can be similarly decomposed into contributions from individual atoms in an ionic material, and to which extent these elements can be transferred from one material to another.

Such a decomposition is performed in equation (6), expressing the Raman susceptibility as a sum of individual atomic contributions proportional to π. However, inspection of table 7 shows that the *same* atoms in two different compounds within the *same* structure and symmetry can exhibit strongly different π. This therefore demonstrates that the computation of individual π tensorial elements is required for each system and that empirical models that would base the computation of the Raman susceptibility on the transfer of the π elements of specific atoms from one material to another would behave very poorly in ferroelectric materials.

11. Conclusions

In this paper, we have calculated, for the first time, the derivative of the linear optical susceptibility with respect to atomic displacement and the second-order nonlinear optical susceptibility tensors of the ferroelectric $BaTiO_3$ and $PbTiO_3$ in their tetragonal phases, and the ferroelectric rhombohedral phase of $BaTiO_3$. These quantities are found to be in good agreement with the available experimental data, leading to an accurate calculation of the Raman spectra of these materials for different experimental configurations. The calculated Raman spectra of the $BaTiO_3$ rhombohedral phase have also been reported for the first time.

The computation of the Raman scattering intensities has been performed not only for the transverse optical modes, but also for the longitudinal optical ones. The agreement between the measured Raman spectra of these prototypical ferroelectrics and the DFT ones is remarkable both for the frequency position and the intensity of the Raman lines. DFT, taking advantage of a recent implementation based on the nonlinear response formalism and the $2n + 1$ theorem, appears as an efficient tool to calculate the Raman spectra of ferroelectric materials, and thus make reasonable predictions on the assignment of their Raman lines.

Finally, this agreement presently demonstrates the state-of-the-art in the computation of Raman responses via the nonlinear formalism on one of the most complex systems, ferroelectrics, and constitutes a step forward in a reliable prediction of their electro-optical responses.

Acknowledgments

Calculations have been performed on the NIC (Université de Liège, Belgium), at CISM (Université Catholique de Louvain, Belgium) and at the Spanish National Supercomputer Center (BSC-CNS, Spain). This work was supported by the VolkswagenStiftung, the European Network of Excellence FAME-NoE and the European strep MaCoMuFi.

References

[1] Hermet P, Goffinet M, Kreisel J and Ghosez Ph 2007 *Phys. Rev.* B **75** 220102(R)
[2] Chiang D P, Peng C H, Mei J K, Jiang I M, Lin S C, Chen Y C, Liu H T, Chen Y F and Tse W S 2008 *J. Raman Spectrosc.* **39** 344
[3] Hasegawa T, Takasu Y, Ogita N, Udagawa M, Yamaura J I, Nagao Y and Hiroi Z 2008 *Phys. Rev.* B **77** 064303
[4] El-Brolossy T A and Talaat H 2008 *J. Raman Spectrosc.* **39** 91
[5] Shim M, Gaur A, Nguyen K T, Abdula D and Ozel T 2008 *J. Phys. Chem.* C **112** 13017
[6] He H Y and Pan B C 2008 *Phys. Rev.* B **77** 073410
[7] Hermet P, Veithen M and Ghosez Ph 2007 *J. Phys.: Condens. Matter* **19** 456202
[8] Hermet P, Izard N, Rahmani A and Ghosez Ph 2006 *J. Phys. Chem.* B **110** 24869
[9] Chadli H, Rahmani A, Sbai K, Hermet P, Rols S and Sauvajol J L 2006 *Phys. Rev.* B **74** 205412
[10] Guha S, Menéndez J, Page J B and Adams G B 1996 *Phys. Rev.* B **53** 13106
[11] Veithen M, Gonze X and Ghosez Ph 2005 *Phys. Rev.* B **71** 125107
[12] Laabidi K, Fontana M D and Jannot B 1990 *Solid Sate Commun.* **76** 765
[13] Perry C H and Hall D B 1965 *Phys. Rev.* B **15** 700
[14] Gonze X and Lee C 1997 *Phys. Rev.* B **55** 10355
[15] Cardona M and Güntherodt G 1982 *Light Scattering in Solids II* (Berlin: Springer)
[16] Johnston W D Jr 1970 *Phys. Rev.* B **1** 3494
[17] Gonze X, Beuken J M, Caracas R, Detraux F, Fuchs M, Rignanese G M, Sindic L, Verstraete M, Zerah G, Jollet F, Torrent M, Roy A, Mikami M, Ghosez Ph, Raty J Y and Allan D C 2002 *Comput. Mater. Sci.* **25** 478
[18] Teter M 1993 *Phys. Rev.* B **48** 5031
[19] Monkhorst H J and Pack J D 1976 *Phys. Rev.* B **13** 5188
[20] Ghosez Ph, Gonze X and Michenaud J P 1996 *Europhys. Lett.* **33** 713
[21] Press W H, Flannery B P, Teukolsky S A and Vetterling W T 1989 *Numerical Recipes (FORTRAN Version)* (Cambridge: Cambridge University Press)
[22] Hughes J L P and Sipe J E 1996 *Phys. Rev.* B **53** 10751
[23] Kleinman D A 1962 *Phys. Rev.* **126** 1977
[24] Wemple S H and DiDomenico D Jr 1972 *Appl. Solid State Sci.* vol 3 (New York: Academic)
[25] Ghosez Ph, Michenaud J P and Gonze X 1998 *Phys. Rev.* B **58** 6224
[26] Harrison W A 1980 *Electronic Structure and the Properties of Solids* (San Fransisco, CA: Freeman)
[27] Gonze X, Ghosez Ph and Godby R W 1995 *Phys. Rev. Lett.* **74** 4035
[28] Ghosez Ph, Gonze X and Godby R W 1997 *Phys. Rev.* B **56** 12811
[29] Loudon R 1964 *Adv. Phys.* **13** 423
[30] Fontana M D, Idrissi H, Kugel G E and Wojcik K 1991 *J. Phys.: Condens. Matter* **3** 8695
[31] Foster C M, Li Z, Grimsditch M, Chan S K and Lam D J 1993 *Phys. Rev.* B **48** 10160
[32] Kwei G H, Lawson A C, Billinge S J L and Cheong S W 1993 *J. Phys. Chem.* **97** 2368
[33] Shirane G, Pepinsky R and Frazer B C 1956 *Acta Crystallogr.* **9** 131
[34] Miller R C 1964 *Phys. Rev.* **134** A1313
[35] Boyd G D, Bridges T J, Pollack M A and Turner E H 1971 *Phys. Rev. Lett.* **26** 387
[36] Miller R C and Nordland W A 1970 *Phys. Rev.* B **2** 4896
[37] Lu H A, Wessels B W, Lin W P, Zhang T G, Wong G K, Neumayer D A and Marks T J 1993 *Appl. Phys. Lett.* **62** 1314
[38] Shumate M S 1996 *Appl. Opt.* **5** 327
[39] Miller R C and Nordland W A 1972 *Phys. Rev.* B **5** 4931
[40] Singh S, Remeika J P and Potopowicz J R 1972 *Appl. Phys. Lett.* **20** 135
[41] Scalabrin A, Chaw A S, Shim D S and Porta S P S 1977 *Phys. Status Solidi* b **79** 731
[42] Nakamura T 1992 *Ferroelectrics* **137** 65